Stem Cell Reports, Volume *10*

Supplemental Information

All-Optical Electrophysiology for High-Throughput Functional Characterization of a Human iPSC-Derived Motor Neuron Model of ALS

Evangelos Kiskinis, Joel M. Kralj, Peng Zou, Eli N. Weinstein, Hongkang Zhang, Konstantinos Tsioras, Ole Wiskow, J. Alberto Ortega, Kevin Eggan, and Adam E. Cohen

Alterations in neuronal excitability in ALS probed through optical electrophysiology studies of human iPSC-derived motor neurons

Evangelos Kiskinis, Joel M. Kralj, Peng Zou, Eli N. Weinstein, Hongkang Zhang, Konstantinos Tsioras, Ole Wiskow, J. Alberto Ortega, Kevin Eggan & Adam E. Cohen

Supplemental Material

Inventory of Supplemental Information

Figures S1 – S6
Tables S1 – S3
Supplemental Discussion
Supplemental Experimental Procedures
Supplemental References

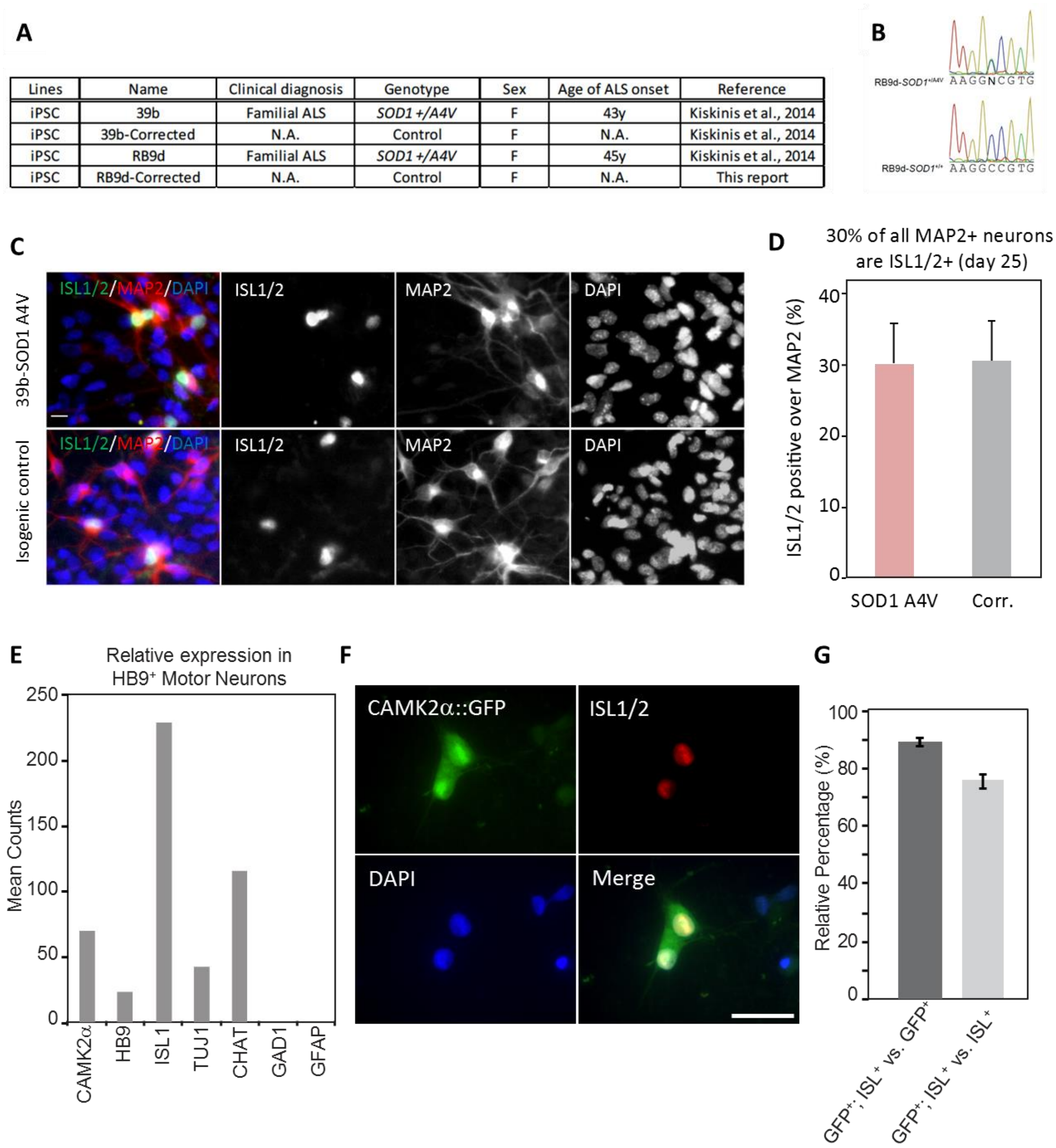

Lines	Name	Clinical diagnosis	Genotype	Sex	Age of ALS onset	Reference
iPSC	39b	Familial ALS	*SOD1 +/A4V*	F	43y	Kiskinis et al., 2014
iPSC	39b-Corrected	N.A.	Control	F	N.A.	Kiskinis et al., 2014
iPSC	RB9d	Familial ALS	*SOD1 +/A4V*	F	45y	Kiskinis et al., 2014
iPSC	RB9d-Corrected	N.A.	Control	F	N.A.	This report

Figure S1. Characterization of human motor neurons derived from iPSCs. Related to Fig. 1. (A) ALS patient-iPSC lines and isogenic controls used in this study. (B) Sequencing chromatographs of exon 1 of SOD1 in patient line RB9d before and after gene-targeting demonstrate the successful correction of the A4V mutation. Editing was performed using Zinc Finger Nucleases as described previously (Kiskinis et al., 2014). (C) Immunocytochemistry for a MN marker (ISL1/2), a pan-neuronal marker (MAP2) and a nuclear marker (DAPI). Scale bar 50 μm. (D) Quantification of MN populations. Error bars represent standard deviation of the percentage of ISL1/2^+ cells from 4 images from 1 differentiation (SOD1 A4V: *n* = 407 $MAP2^+$ cells; Corrected: *n* = 291 $MAP2^+$ cells). (E) Analysis of previously published RNA-Seq data from iPSC-derived $HB9^+$ MNs purified via FACS (Kiskinis et al., 2014; GEO entity: GSE54409). These cells expressed CAMK2α, HB9, TUJ1 and CHAT, while the glial marker GFAP and the interneuron marker

GAD1 were absent. (F) Immunocytochemistry to detect the selectivity and specificity in MNs of lentivirally delivered constructs with the CamKIIα promoter. Images show MN cultures infected with lentivirus containing CamKIIα-driven eGFP. Cells were labelled by immunocytochemistry with antibodies for ISL1/2 and eGFP, and DAPI; scale bar 30 μM. (G) Quantification of images as in (E). 89% of eGFP$^+$ cells were also ISL$^+$. 75% of all ISL$^+$ MNs were also eGFP$^+$. Error bars represent s.e.m. from 42 images taken from 2 independent differentiations, *n* = 1147 ISL$^+$ human iPSC-MNs.

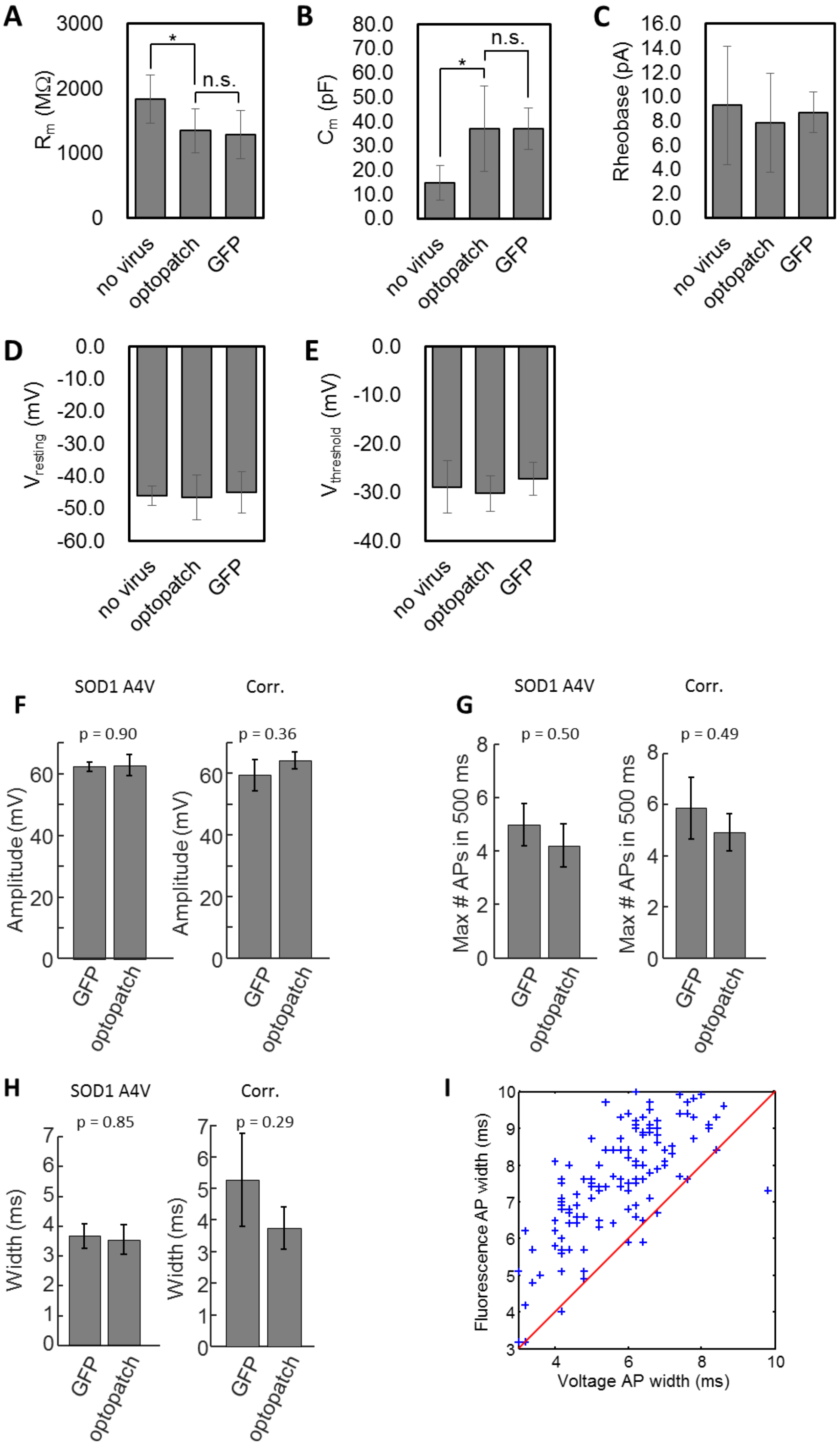
A
3000
2000
1000
0
R_m (MΩ)
*
n.s.
no virus
optopatch
GFP
B
80.0
70.0
60.0
50.0
40.0
30.0
20.0
10.0
0.0
C_m (pF)
*
n.s.
no virus
optopatch
GFP
C
16.0
14.0
12.0
10.0
8.0
6.0
4.0
2.0
0.0
Rheobase (pA)
no virus
optopatch
GFP
D
0.0
-10.0
-20.0
-30.0
-40.0
-50.0
-60.0
$V_{resting}$ (mV)
no virus
optopatch
GFP
E
0.0
-10.0
-20.0
-30.0
-40.0
$V_{threshold}$ (mV)
no virus
optopatch
GFP
F
SOD1 A4V
p = 0.90
Amplitude (mV)
60
40
20
0
GFP
optopatch
Corr.
p = 0.36
Amplitude (mV)
60
40
20
0
GFP
optopatch
G
SOD1 A4V
p = 0.50
Max # APs in 500 ms
8
6
4
2
0
GFP
optopatch
Corr.
p = 0.49
Max # APs in 500 ms
8
6
4
2
0
GFP
optopatch
H
SOD1 A4V
p = 0.85
Width (ms)
7
6
5
4
3
2
1
0
GFP
optopatch
Corr.
p = 0.29
Width (ms)
7
6
5
4
3
2
1
0
GFP
optopatch
I
Fluorescence AP width (ms)
10
9
8
7
6
5
4
3
Voltage AP width (ms)
4
6
8
10

Figure S2. Validation of Optopatch measurements in iPSC-MNs. Related to Fig. 2. **(A-E)** Effect of Optopatch expression on baseline electrophysiology. Comparisons between iPSC-MNs expressing no lentivirus, Optopatch constructs, or an eGFP control showed no significant differences between Optopatch and eGFP expression in **(A)** membrane resistance, **(B)** membrane capacitance, **(C)** rheobase current, **(D)** resting potential, and **(E)** action potential initiation threshold (See Table S1). The CaMKIIα promoter targeted expression (of either eGFP or Optopatch) to more mature, and hence larger MNs (Prè et al., 2014), leading to smaller membrane resistance and larger membrane capacitance compared to non-transduced cells. Error bars represent s.e.m.. Measurements were on n = 10 – 14 cells per condition. **(F – H)** Comparison of spiking parameters in iPSC-MNs expressing either Optopatch constructs or an eGFP positive control, as recorded by manual patch clamp. Current was injected in 500 ms pulses of nineteen amplitudes (5 pA to 95 pA; n = 8 39b-Cor cells with eGFP, n = 15 39b-Cor cells without Optopatch, n = 9 39b cells with eGFP and n = 9 39b cells with Optopatch). **(F)** Within each genotype, cells that expressed eGFP and those that expressed Optopatch had indistinguishable average action potential amplitude (p = 0.90 for 39b, p = 0.36 for 39b-Cor, unpaired t-test). **(G)** The cells reached indistinguishable maximum firing rates (p = 0.50 for 39b, p = 0.49 for 39b-Cor, unpaired t-test). **(H)** The width of the spikes at rheobase was indistinguishable (p = 0.85 for 39b, p = 0.29 for 39b-Cor, unpaired t-test). **(I)** Comparison of action potential width measured optically vs. electrically. Optical measurements reported an AP width that was greater than the electrically recorded width by 1.8 ± 1.1 ms (mean ± s.d.; n = 148 spikes, 4 cells).

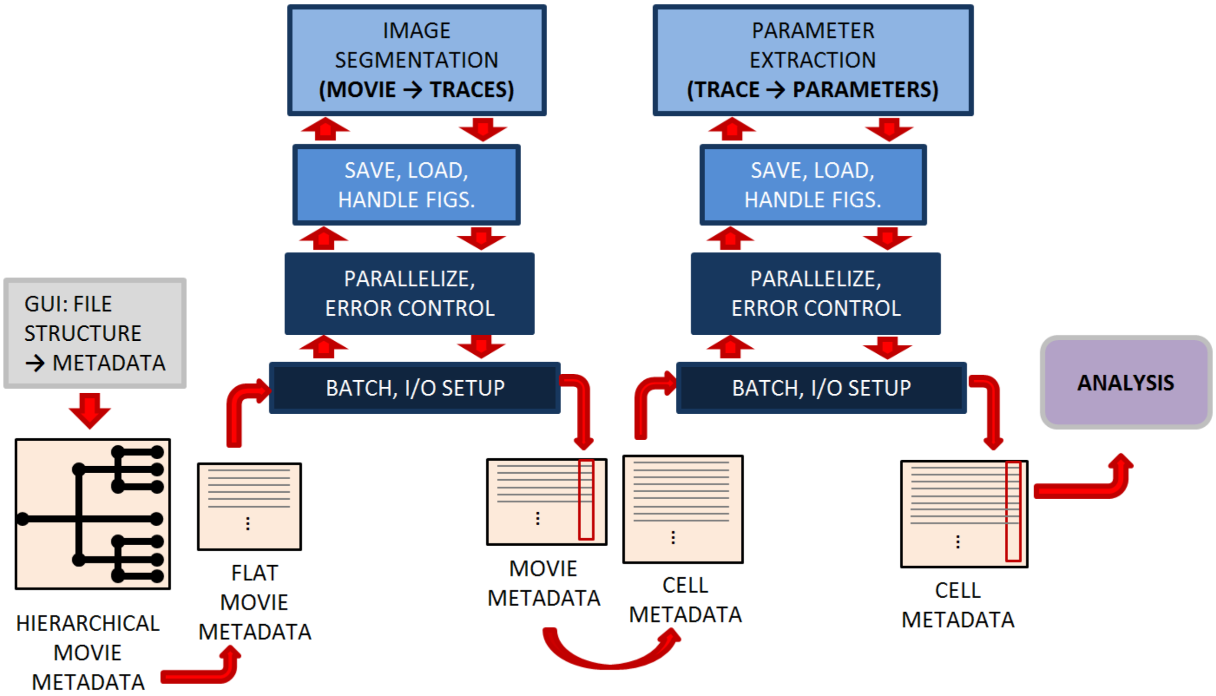

Figure S3. Data pipeline for image segmentation and spike parameterization. Related to Fig. 2. Metadata from each experiment and sub-experiment is created using a graphical user interface. The hierarchically organized metadata is then flattened into a matrix listing each recording and its associated metadata. This organization facilitates parallel analysis on a computer cluster. In the first stage of analysis, movies are translated into a set of fluorescence traces via image segmentation; morphological and expression level measurements are also recorded. Summary figures of each movie's analysis are created and data from each movie's analysis is saved individually. The metadata is then broken up by cell (rather than by movie) and sent to the parameter extraction pipeline which again is parallelized. In this stage, each cell's fluorescence trace is loaded and parameterized. A summary figure is created and again the results are saved individually. The final list of cells and their parameterizations can then be loaded for further analysis. The entire pipeline is implemented in MATLAB and run on the Odyssey Research Computing cluster at Harvard University.

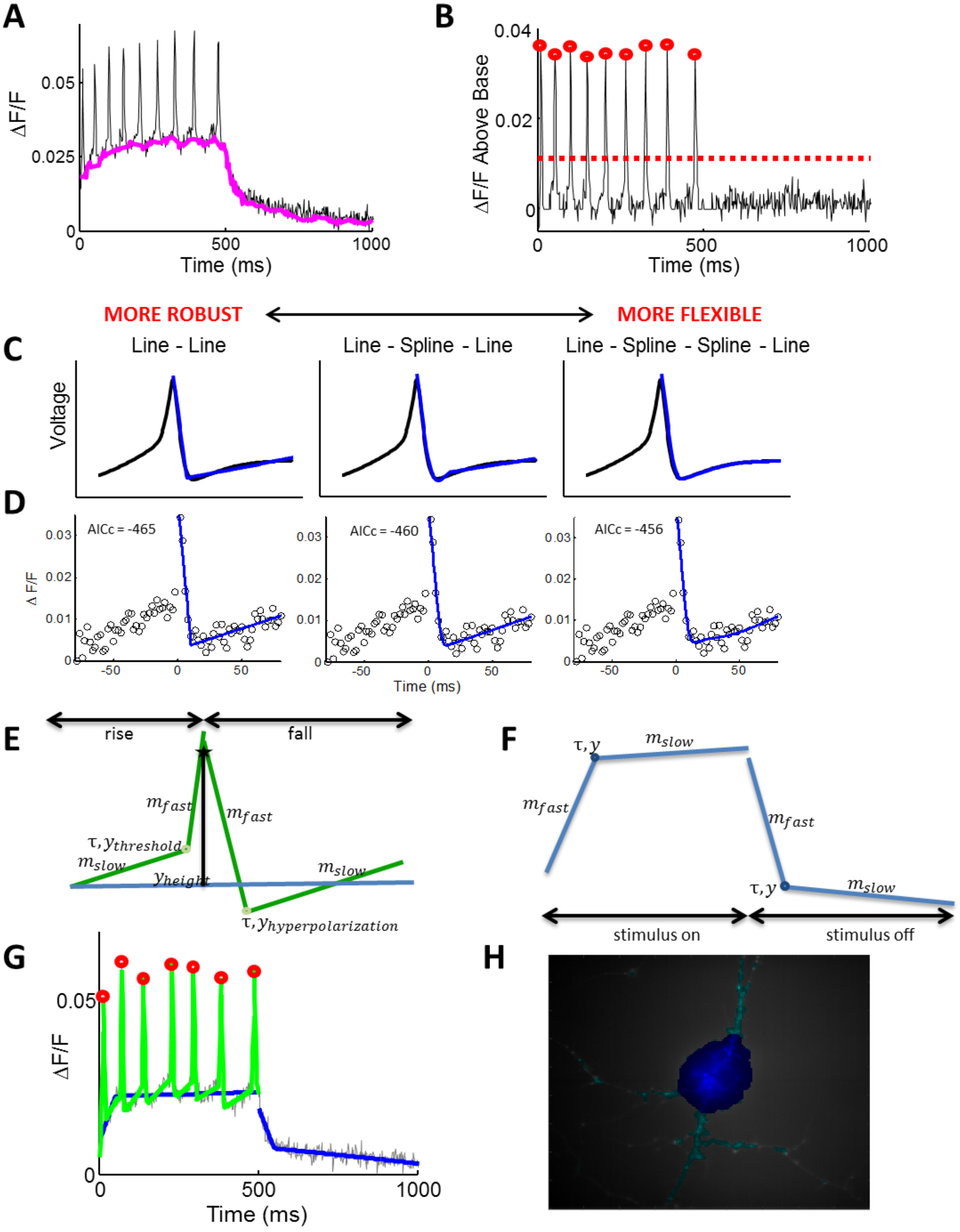

Figure S4. Data reduction and parameterization of spiking waveforms. Related to Fig. 2. **(A)** Fluorescence traces were temporally filtered with a specialty ordinal filter to separate spikes from baseline (window size of 20 ms, 40th percentile taken as baseline estimate). **(B)** A threshold for spike identification was set based on an estimate of the noise. **(C – F)** Information-theoretic determination of optimal parameterization of optically recorded spike waveforms. We created a hierarchy of models with different number of parameters; adding more parameters increased flexibility but decreased robustness to noise. The least complex model of the AP downstroke consisted of two lines meeting at a point. The next model added one spline joining the two lines. The most flexible model contained two splines. **(C)** Fit of each model to an AP waveform recorded by manual patch clamp.(Bean, 2007) **(D)** Fit of each model to single-trial Optopatch data. Corrected Akaike's information criterion (AICc) balances the quality-of-fit with the complexity of the model. Lower scores indicate a better model for the given data. In this example (as in 95% of tests), AICc was lowest for the least complex and most robust two-line model. **(E)** Parameterization of optically recorded action potential waveforms **(F)** and baseline waveforms. **(G)** Final parameterization, consisting of the fitted baseline and action potential models. **(H)** Automated identification of soma (dark blue) and processes (cyan) calculated from the activity-based map of the single-cell profile.

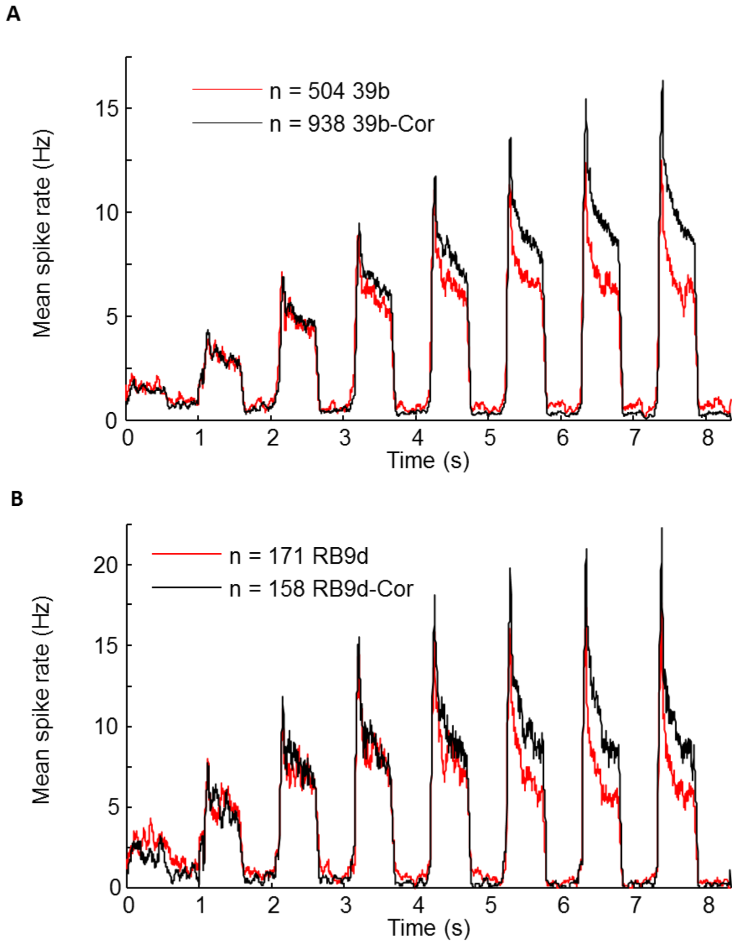

Figure S5. Replication of core experimental results in two distinct isogenic pairs. Related to Fig. 3. A) The 39b SOD1(A4V) line and its isogenic corrected pair. B) The RB9d SOD1(A4V) line and its isogenic corrected pair. As in the 39b cell line, the SOD1 (A4V) cells showed hyperexcitability under weak stimulus, but hypo-excitability under strong stimulus.

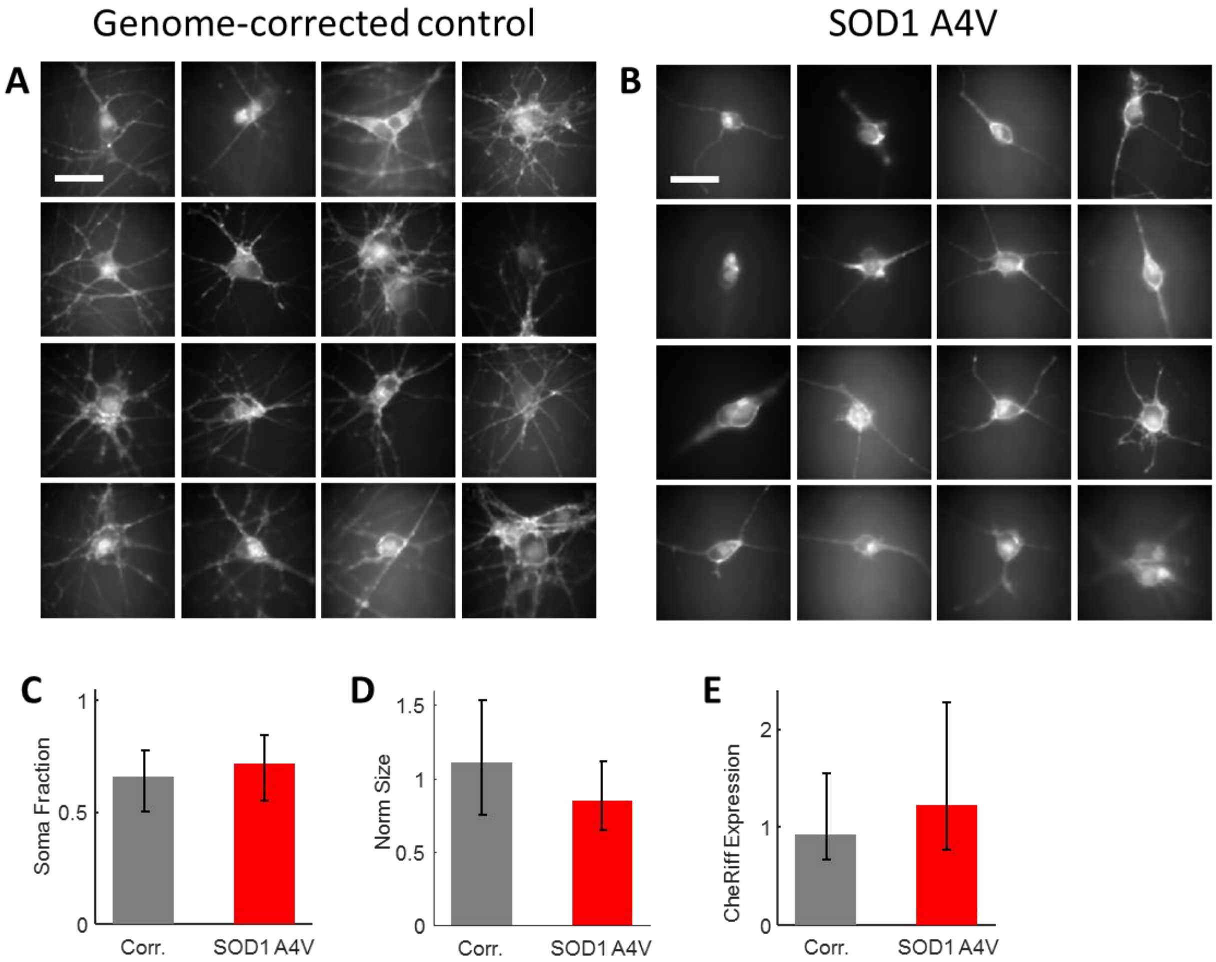

Figure S6. Morphological differences between control and SOD1 A4V motor neurons. Related to Fig. 3. Images show **(A)** corrected control and **(B)** *SOD1* A4V mutant iPSC-MN. Fluorescence is from QuasAr2. Scale bars in (A) and (B) 20 µm. **(C)** Median fraction of the cell area occupied by soma (as opposed to dendrite) in the control and mutant iPSC-MNs; error bars show the 25th and 75th percentiles of the population. The difference between the two populations was significant to $p = 1\times10^{-10}$ (0.66 in control, 0.72 in mutant, unpaired t-test). **(D)** Median size of the control and mutant cell somas, normalized to the population median; error bars show 25th and 75th percentile. The difference between the two populations was significant to $p = 8\times10^{-17}$ (1.11 a.u. in control, 0.84 in mutant, unpaired t-test). **(E)** Difference in median CheRiff expression level between control and mutant cells, normalized to the whole population median. Error bars shows the 25th and 75th percentile. The difference between the two populations is significant (0.92 a.u. in control, 1.22 in mutant, $p = 2\times10^{-5}$, unpaired t-test). In C – E, control *n* = 843 cells, mutant *n* = 331 cells.

	no virus		Optopatch		eGFP	
	mean	std. dev.	mean	std. dev.	mean	std. dev.
R_m (MΩ)	1829	374	1345	339	1284	375
C_m (pF)	14.9	7.1	37.0	17.5	37.0	8.5
Resting potential (mV)	-46.2	3.0	-46.6	6.9	-45.0	6.4
Threshold potential (mV)	-28.9	5.4	-30.2	3.6	-27.3	3.4
Rheobase (pA)	9.2	4.9	7.8	4.1	8.7	1.7

Table S1. Comparison of electrophysiological parameters of iPSC-MN infected with either no virus, CaMKIIa-driven Optopatch, or CaMKIIa-driven eGFP. The data are shown graphically in Fig. S2.

SOD1 A4V – Corr. Difference

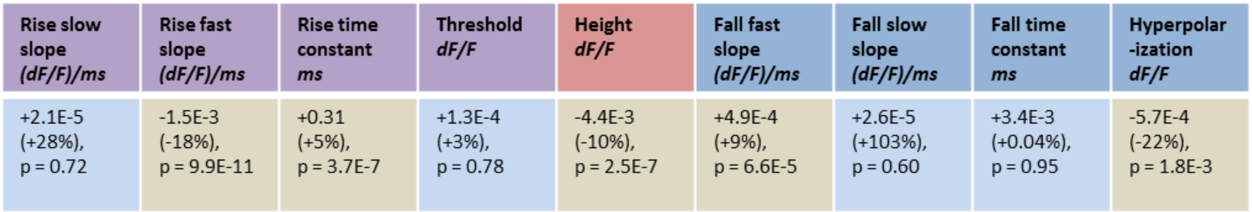

Rise slow slope *(dF/F)/ms*	Rise fast slope *(dF/F)/ms*	Rise time constant *ms*	Threshold *dF/F*	Height *dF/F*	Fall fast slope *(dF/F)/ms*	Fall slow slope *(dF/F)/ms*	Fall time constant *ms*	Hyperpolar -ization *dF/F*
+2.1E-5 (+28%), p = 0.72	-1.5E-3 (-18%), p = 9.9E-11	+0.31 (+5%), p = 3.7E-7	+1.3E-4 (+3%), p = 0.78	-4.4E-3 (-10%), p = 2.5E-7	+4.9E-4 (+9%), p = 6.6E-5	+2.6E-5 (+103%), p = 0.60	+3.4E-3 (+0.04%), p = 0.95	-5.7E-4 (-22%), p = 1.8E-3

Change with Number of APs per Stimulus

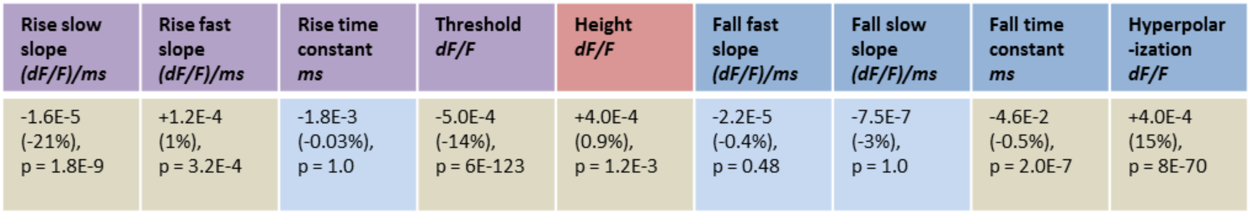

Rise slow slope *(dF/F)/ms*	Rise fast slope *(dF/F)/ms*	Rise time constant *ms*	Threshold *dF/F*	Height *dF/F*	Fall fast slope *(dF/F)/ms*	Fall slow slope *(dF/F)/ms*	Fall time constant *ms*	Hyperpolar -ization *dF/F*
-1.6E-5 (-21%), p = 1.8E-9	+1.2E-4 (1%), p = 3.2E-4	-1.8E-3 (-0.03%), p = 1.0	-5.0E-4 (-14%), p = 6E-123	+4.0E-4 (0.9%), p = 1.2E-3	-2.2E-5 (-0.4%), p = 0.48	-7.5E-7 (-3%), p = 1.0	-4.6E-2 (-0.5%), p = 2.0E-7	+4.0E-4 (15%), p = 8E-70

Change with Increasing Stimulus at Maximum Firing Rate

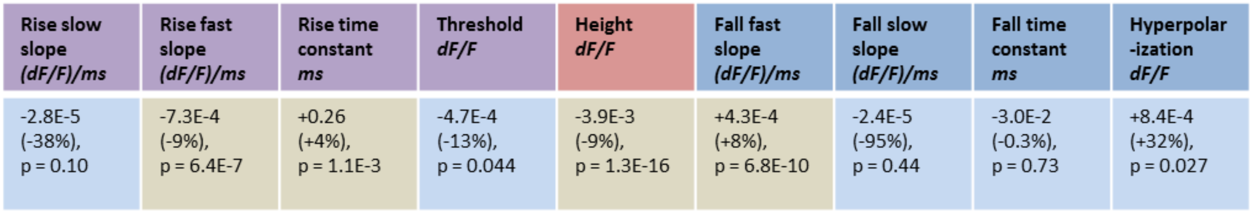

Rise slow slope *(dF/F)/ms*	Rise fast slope *(dF/F)/ms*	Rise time constant *ms*	Threshold *dF/F*	Height *dF/F*	Fall fast slope *(dF/F)/ms*	Fall slow slope *(dF/F)/ms*	Fall time constant *ms*	Hyperpolar -ization *dF/F*
-2.8E-5 (-38%), p = 0.10	-7.3E-4 (-9%), p = 6.4E-7	+0.26 (+4%), p = 1.1E-3	-4.7E-4 (-13%), p = 0.044	-3.9E-3 (-9%), p = 1.3E-16	+4.3E-4 (+8%), p = 6.8E-10	-2.4E-5 (-95%), p = 0.44	-3.0E-2 (-0.3%), p = 0.73	+8.4E-4 (+32%), p = 0.027

Table S2. Changes in action potential waveform parameters between *SOD1* A4V and genome corrected controls (see Figure S5 for definitions). We performed a linear regression to determine the factors that influenced average waveform parameters for each stimulus and each cell, up to the stimulus at which the maximum firing rate first occurred. The control parameters were: cell line (mutant or control, a categorical variable), number of action potentials in the stimulus epoch, stimulus strength (to control for blue light-induced photoartifacts), and dish recording day (to control for day-to-day variability). Each column of the **SOD1 A4V - Corr. Difference** table lists the regression coefficient for genotype (mutant vs. control), the percent change relative to the control's average, and the p value from the regression coefficient t-test. Coefficients are highlighted in olive-green which are significant to an α = 0.01 threshold after Holm-Bonferroni multiple hypothesis correction (9 hypotheses from the 9 parameters).

	Rise slow slope *(dF/F)/ms*	**Rise fast slope** *(dF/F)/ms*	**Rise time constant** *ms*	**Threshold** *dF/F*	**Height** *dF/F*	**Fall fast slope** *(dF/F)/ms*	**Fall slow slope** *(dF/F)/ms*	**Fall time constant** *ms*	**Hyperpolar-ization** *dF/F*
K_V7	+4.4E-5 (+35%) β = 0.20	+1.7E-3 (+15%) β = 0.24	-7.0E-1 (-12%) β = -0.20	+2.2E-3 (+132%) β = 0.68	+6.0E-3 (+11%) β = 0.49	-1.5E-3 (-15%) β = -0.23	+1.0E-5 (+25%) β = 0.05	-3.2E-1 (-5%) β = -0.09	-1.5E-3 (-109%) β = -0.63
K_{dr}	+1.6E-4 (+128%) β = 0.67	+1.4E-3 (+13%) β = 0.18	-8.4E-1 (-15%) β = -0.23	+4.2E-3 (+253%) β = 1.26	+3.6E-3 (+6%) β = 0.29	-5.7E-3 (-57%) β = -0.96	+1.9E-4 (+468%) β = 0.78	-2.4 (-39%) β = -0.81	-3.8E-3 (-267%) β = -1.35
Na	+8.7E-5 (+67%) β = 0.10	+2.4E-2 (+211%) β = 1.81	-5.8 (-102%) β = -1.13	+1.9E-3 (+117%) β = 0.30	+4.1E-2 (+73%) β = 2.44	-1.6E-2 (-165%) β = -1.76	+9.9E-6 (+24%) β = 0.01	-4.6 (-74%) β = -1.05	+8.5E-4 (+60%) β = 0.16

Table S3. Change in action potential waveform in numerical simulations with increases in channel conductance. For each channel or set of channels, simulations were run with a range of conductances and a range of optogenetic stimulus strengths corresponding to changes in channelrhodopsin conductance ($\boldsymbol{g_m}$, see Fig. 6). The simulated voltage trace was down-sampled to match the data acquisition frame rate (500 Hz), and action potentials were fit with the same set of parameters used in the fluorescence data. We then fit a linear regression on the average waveform parameter from each step with control variables for the channel conductance and the input conductance. Rows of the table show the regression coefficient (in units of waveform parameter per base simulation conductance) for variations in K_V7, delayed rectifier K_V, and Na_V. The coefficient as a percentage of the base simulation average is shown in parenthesis. As another indicator of the strength of the relationship we also show the coefficient as a fraction of its standard deviation, β (we can write $\beta = \frac{T}{\sqrt{N-3}}$ where T is the t-statistic and $N-3$ is the number of degrees of freedom in our regression).

Supplemental Discussion

Optical crosstalk in Optopatch measurements

The fluorescence signal showed a slow increase in baseline during each optical stimulus epoch (Fig. 1D). This increase did not occur in patch clamp recordings with optical stimulation, indicating that the increase did not correspond to a real increase in membrane potential. The increase also did not occur in optical recordings with stimulation via current injection from the patch pipette, indicating that the increase was not a slow response of the voltage indicator to membrane depolarization. The increase only occurred with simultaneous blue light stimulation and fluorescence imaging. These observations implied that the increase in baseline fluorescence was due to blue light photo-production of a fluorescent product. This effect was not observed in prior experiments with rodent primary neurons due to higher CheRiff expression in the rodent cells (and consequently lower blue light intensities), and better membrane trafficking of QuasAr2 in the rodent cells.

Spike parameterization and model reduction

In functional fitting, choosing a good functional form is critical. On the one hand, it must be capable of fitting the data well and providing a meaningful description of relevant parameters; on the other hand, it must be robust and avoid over-fitting. We first attempted to fit action potential data with exponential rise and decay functions, but the fit was often qualitatively poor. We found more success with combinations of lines and splines. For instance, to describe the shape of an action potential after its peak, one line could be used to fit the fast action potential down-stroke, a connected spline segment to model the after-hyperpolarization, and then another connected line to fit the return to baseline (Fig. S4).

To address the problem of robustness and overfitting we employed an information-theoretic model reduction scheme. Our line-spline-line functions lent themselves well to the creation of a hierarchy of models with varying degrees of complexity (Fig. S4). We tested three models, with zero, one, or two splines between two lines. The point at which each segment (line or spline) joined with the next was allowed to vary along both the ΔF and time axes, but continuity between segments was enforced. These models had four, six and eight parameters respectively: the slope of the two lines and position of one, two, or three joining points.

To balance the tradeoff between quality-of-fit and model complexity we employed corrected Akaike information criteria (AICc).(Burnham and Anderson, 2003) This criterion enabled us to choose the model with the best level of complexity for our data, based on how closely the data matched the model, how many parameters must be fit in the model, and how many data points are being fit.

Our likelihood function assumed Gaussian noise in ΔF; the width of the distribution was estimated by subtracting a median filtered copy of each cell's recording (to remove baseline fluctuations) and then taking the 50^{th} minus the 16^{th} percentile in the residual. We fit a sample of 200 action potentials randomly selected from 50 cells using the three models. Although these functional models describe action potential shape well both pre- and post-peak, we focused on post-peak since after-hyperpolarization is in general more difficult to describe. The results from AICc showed that the simplest model (0 splines) was optimal in 95% of sample action potentials, versus 3% for the one-spline model and 2% for the two-spline model. We therefore used the simplest model. We fit the pre- and post-peak sections of each action potential separately to a pair of lines which could vary in their slope and the point at which they met (Fig. S4). We called this model a “variable hinge.”

AP waveform statistics

We studied action potential waveforms in the pre-depolarization block regime. Here, after the first two spikes upon stimulus onset, cells typically settled into a consistent limit cycle with little change in action potential waveform over the course of the stimulus (Fig. 5). We therefore averaged together the parameters of the waveforms of each action potential after the first 100 ms of stimulation.

As action potential firing rate increased, action potential waveforms changed. We constructed a linear model for each average action potential waveform parameter from each step stimulus, with a control coefficient for the number of action potentials in the step from which the waveform was taken. To control for any residual variation caused by blue light crosstalk, we also included a control coefficient for the stimulus number in our linear model. To study differences between control and mutant lines, we added a categorical variable to the model for cell line (this variable was non-interacting with the others). The model was fit to a dataset containing waveform parameters from every step in every cell up to and including the first step at which the maximum firing rate was reached. In reporting parameters that changed significantly between the two populations, we applied the Holm-Bonferroni method to correct for multiple hypothesis testing (see Methods). Regression coefficients and p values are presented in Table S2.

We compared the set of differences and similarities between action potential waveforms from mutant and control cells to other axes of variability between action potential waveforms. The set of genotype-dependent changes was different from those which occurred as the firing rate increased (Table S2). Genotype-dependent changes were nearly identical, however, to the set of changes which occurred as one moved from the first stimulus at which the maximum firing rate was reached to the last stimulus at which the maximum firing rate occurred before depolarization block (Table S2). This observation suggests that the differences in waveform between control and mutant cell lines may come from the same mechanism that produced differences in the probability of depolarization block.

Supplemental Experimental Procedures

Immunocytochemistry

Cell cultures were fixed in 4% PFA for 15 min at 4 °C, permeabilized with 0.2% Triton-X in PBS for 2 hours and blocked with 10% donkey serum in PBS-T (Triton 0.1%). Cells were then incubated in primary antibody overnight and secondary antibodies for 1 hour in 2% donkey serum in PBS-T after several washes in between. DNA was visualized by a Hoechst stain. The following antibodies were used: Islet1 (1:200, DSHB, 40.2D6), TUJ1 (1:1000, Sigma, T2200), MAP2 (1:10000, Abcam ab5392), GFP (1:500, Life Technologies, A10262). Secondary antibodies used (488, 555, 594, and 647) were AlexaFluor (1:1000, Life Technologies) and DyLight (1:500, Jackson ImmunoResearch Laboratories).

Virus production

Lentivirus was produced in HEK293-T cells from previously described plasmids(Hochbaum et al., 2014) DRH334 (CamKIIα-QuasAr2, Addgene plasmid 51692) and DRH313 (CamKIIα-CheRiff, Addgene plasmid

51693). HEK293-T cells were grown in 15 cm dishes to ~50% confluence at 37 °C and 5% CO_2. Transfection of each gene, as well as packaging and coat proteins (psPAX2 and VSVg, respectively), was performed with poly-ethylenimine (PEI). For each 15 cm dish, a cocktail of 22 μg psPAX2, 16 μg gene, and 10 μg VSVg was suspended in 500 μL of Optimem. PEI was added to the Optimem mixture (140 μL from a 1 mg/mL stock) and vortexed briefly to mix. The mixture was incubated at room temperature for 15 minutes. After incubation, 25 mL of pre-warmed DMEM was added to the DNA/PEI mixture and gently mixed. Medium was aspirated off the 15 cm plate and the DNA/PEI/DMEM mixture was added gently onto the cells and the plate was returned to the incubator. After 48 hours, the supernatant was collected and spun for 5 minutes at 1200 g to pellet any collected cells. The supernatant was then filtered through a 0.45 μm filter, aliquoted into 1.5 mL volumes, and frozen at -80 °C.

Gene delivery

Approximately 40,000 cells of differentiated motor neuron cultures were plated on poly-D-lysine/laminin-coated 35 mm glass bottom dishes (MatTek) for Optopatch recordings. Each dish was transduced with lentiviruses 7-10 days before scheduled recording times. A mixture of 200 μL of QuasAr2 and 70 μL of CheRiff lentiviruses were combined with 200 μL of the complete neurobasal medium, added onto the cells and left overnight in the incubator. The next morning the virus mixture was removed, plates were washed and replenished with fresh, complete neurobasal medium.

Data analysis

Data cleaning

Under external synchronous triggering, the Flash 4.0 camera rounds the exposure time to the nearest 10 μs. This variation in exposure time is inconsequential for long exposures, but led to spurious noise of 0.5% at an exposure time of 2 ms, due to the asynchronicity of the computer clock triggering the camera and the camera's internal clock. We used the whole-field image intensity to estimate this rounding error and then divided the pixel values in each frame by the estimated exposure time to correct for the variation in exposure time.

Image processing and segmentation

Our image segmentation pipeline was adapted from that of Mukamel and coworkers (Mukamel et al., 2009) and consisted of pre-process filtering, PCA-ICA in the time domain, and post-process statistical analysis. A key technical challenge in the analysis was that each pixel had a low signal-to-noise ratio (SNR) due to the short exposure time (2 ms) and the low intrinsic brightness of QuasAr2. Noise from neighboring pixels was uncorrelated, while true signals from neighboring pixels tended to be correlated because each cell extended over many pixels. We thus started the analysis by performing median spatial filtering to improve the per-pixel signal-to-noise ratio. This procedure also removed the effect of sparse bad pixels in the camera image sensor.

A second key challenge was that the dominant fluorescence dynamics corresponded to (a) whole-field photobleaching, and (b) stepwise increases and decreases in whole-cell fluorescence triggered by the blue stimulus illumination. Both of these sources of temporal variation were highly correlated between cells and thus were not good signals for activity-based image segmentation. Single-cell spiking patterns, however, were statistically independent between cells and provided a robust segmentation signal. We therefore applied high-pass filtering in the time domain with a mean-subtracted Gaussian filter set to accentuate action potentials (window size of 20 ms, Gaussian with standard deviation of 3 ms).

A third key challenge was that the signals of interest were sparse in space and time, while the noise was broadly distributed. The PCA-ICA protocol involved calculations of cross-correlation functions. Inclusion of noise-dominated elements of the data in these calculations led to increases in noise without improvements in beneficial signal. We therefore chose only to apply PCA-ICA to the region in time corresponding to our staircase stimulation, rather than including the spontaneous imaging region, since most activity occurred during stimulation.

Using the notation $A_{x,y}$ for matrices where *x* and *y* represent the domains a matrix maps *from* and *to* respectively, these last two steps translated a movie matrix $M_{r,T}$ (where *r* is the pixel domain and *T* is the time domain) into a high-pass-filtered and abbreviated movie matrix $H_{r,t}$ (where *t* is the abbreviated time domain).

There were fewer frames than pixels in our movies, so we employed time-domain-covariance matrix PCA to reduce dimensionality of the data. The covariance matrix $H_{r,t}{}^{\intercal} H_{r,t}$ was decomposed into its eigenvectors E with eigenvalues in the diagonal matrix D; the twenty with the largest eigenvalues were retained to form the eigenvector/principal component matrix $E_{t,p}{}^{\intercal}$ (where *p* is the principal component index). We applied ICA to the matrix $E_{t,p}{}^{\intercal}$ using the FastICA algorithm with a symmetric approach. The expected distribution of fluorescence values for each pixel was a Gaussian (noise) with a one-sided long tail (action potentials). This distribution has high skew and so we employed the function $g(u) = u^3$ as a contrast function.(Hyvärinen and Oja, 2000) Six independent components, $C_{t,v}$, were calculated, but these did not correspond to true neuronal activity waveforms because they were extracted from the temporally high-pass-filtered movie.

ICA produced a separation matrix $S_{p,v}$ which mapped from the principal component domain to the ICA temporal voices domain (*v*), i.e. $C_{t,v} = E_{t,p} S_{p,v}$, We generated a spatial filter $F_{r,v}$ which mapped from the spatial pixel domain to the spatial voices domain:

$$F_{r,v} = H_{r,t} E_{t,p} D^{-1} S_{p,v}.$$

Application of this filter to each frame of the original movie provided a final fluorescence trace, $\mathrm{T}_{v,T}$, for each cell in the movie, i.e. $\mathrm{T}_{v,T} = F_{r,v}{}^{\intercal} M_{r,T}$.

Once the traces were constructed, we performed spike finding (see below). Traces with five or fewer spikes in the entire recording were considered to be either noise or inactive cells and were discarded. A common failure mode for ICA produced traces with positive spikes on top of an inverted baseline. These were also automatically discarded by checking for negative changes in baseline during high stimulus.

We also extracted an image of each cell, $I_{r,v}$, by cross-correlating the high-pass-filtered time-trace of each cell with the high-pass-filtered movie, i.e. $I_{r,v} = H_{r,t} C_{t,v}$. Cells may be partially overlapping but they are still spatially sparse in the sense that they typically only cover a relatively small region of the whole frame. The distribution of values in $I_{r,v}$ comprised Poisson-distributed background noise, with a long tail corresponding to the cell. We set a dynamic threshold of 1.8 times the estimated Poisson parameter λ to determine which pixels were most likely to be on-cell. The final cell mask for a given cell v_j was then given by $R_{r_i,v_j} = \mathrm{I}[I_{r_i,v_j} > 1.8 * \frac{\left(\sum_{k=1}^{r_{\max}} I_{r_k,v_j}\right)}{r_{max}}]$ where I is the indicator function and r_{max} is total number of pixels.

Morphological analysis and calibration of ΔF/F

The PCA-ICA method described above produced traces which were scaled and offset versions of the true fluorescence trace; while this is acceptable for spike-counting, comparison of spike waveforms required an estimate of the underlying fractional change in fluorescence, ΔF/F. To the extent that resting potentials were approximately the same between cells, ΔF/F provided a measure of relative changes in voltage and thus enabled comparisons of spike amplitude and after-hyperpolarization.

A naïve algorithm would simply fit the clean but uncalibrated ICA-generated trace to a noisy trace with true ΔF/F generated from averaging the raw signal over the entire area of the cell. That is, we might take the average trace $A_{v_k,T} = R^{\intercal}_{r,v_k} M_{r,T}$ for a given cell and scale the uncalibrated trace to match: $\mathrm{T}'_{v_k,T} = \hat{a}\,\mathrm{T}_{v_k,T} + \hat{b}$ where $\hat{a}, \hat{b} = \mathrm{argmin}_{a,b}\left(\sum_{i=1}^{T_{max}} \left(a\,\mathrm{T}_{v_k,T_i} + b - A_{v_k,T_i}\right)^2\right)$. Then the baseline (the F in ΔF/F) would come from low pass filtering this new trace $\mathrm{T}'_{v_k,T}$, and spikes (the ΔF) would be measured relative to this baseline. The problem is that the average trace $A_{v_k,T}$ may contain crosstalk from other cells. We therefore sought a better way to estimate an unbiased offset and amplitude for the fluorescence signal.

Instead of using the entire cell mask ($R_{r,v}$) to calculate $A_{v,T}$, we identified spatial regions which were unobstructed by neighboring cells. For a cell indexed by v_k we calculated the "pure" mask by excluding all the pixels at which other cells were present:

$$P_{r,v_k} = \left(1 - R_{r,v_1}\right) \odot \left(1 - R_{r,v_2}\right) \odot \ldots \odot \left(1 - R_{r,v_{k-1}}\right) \odot\ R_{r,v_k} \odot \left(1 - R_{r,v_{k+1}}\right)\ \odot \ldots \odot \left(1 - R_{r,v_{max}}\right)$$

where $\odot$ represents elementwise multiplication. In certain rare cases a cell had no regions which were not shared by others. These cells were excluded. To further refine our mask, we identified those pixels within the pure region which matched the ICA-derived trace as closely as possible. We first high pass filtered the movie and the ICA-derived trace in the time domain with a mean-subtracted Gaussian filter set to accentuate action potentials (window size of 20 ms, Gaussian with standard deviation of 3 ms), giving the movie $M^f_{r,T} = P^{\intercal}_{r,v} M_{r,T} \otimes G_T$ and the trace $T^f_{v,T} = \mathrm{T}_{v,T} \otimes G_T$ where $\otimes$ represents a convolution and G_T represents the temporal filter. Following the maximum likelihood pixel weighting algorithm described in Kralj *et al.* (Kralj et al., 2012), we calculated for each pixel of the movie a set of coefficients describing the best fit (by a least squares error) of the ICA-derived trace to the pixel trace. The error on this best fit, normalized the variance of the pixel's signal, gives an indicator of quality-of-fit: $\zeta_{r,v_k} = \frac{\min_{a,b}\left(\sum_{i=1}^{T_{max}}\left(a\,\mathrm{T^f}_{v_k,T_i} + b - M^f{}_{v_k,T_i}\right)^2\right)}{\sum_{i=1}^{T_{max}}\left(M^f{}_{v_k,T_i} - \frac{1}{T_{max}}\sum_{i=1}^{T_{max}} M^f{}_{v_k,T_i}\right)^2}$. Our final mask was then $Z_{r_i,v_k} = \frac{1}{\sum \frac{1}{\zeta_r}} \begin{cases} 1/\zeta_{r_i} & P_{r_i,v_k} = 1 \\ 0 & P_{r_i,v_k} = 0 \end{cases}$. At last, we can construct a new average trace: $A'_{v_k,T} = Z^{\intercal}_{r,v_k} M_{r,T}$ for each cell and perform the fit $\hat{a}, \hat{b} = \mathrm{argmin}_{a,b}\left(\sum_{i=1}^{T_{max}}\left(a\,\mathrm{T}_{v_k,T_i} + b - A'_{v_k,T_i}\right)^2\right)$ to obtain a trace with real fluorescence units, $\mathrm{T}'_{v_k,T} = \hat{a}\,\mathrm{T}_{v_k,T} + \hat{b}$.

This fluorescence signal still contained artifacts from photobleaching. We estimated the photobleaching baseline using a filter that took the minimum in a sliding window of duration 1 s. Dividing the fluorescence signal by this photobleaching estimate at each time point provided our final ΔF/F trace.

Estimating morphological parameters

We also used the cell mask, R_{r,v_j}, to study the structural morphology of each neuron (see *Morphological analysis* above*)*. Soma and dendrite can be distinguished on the basis of how "thin" they are: pixels on the soma are likely to be surrounded by other on-cell pixels, while pixels on the dendrite are more likely to be adjacent to off-cell pixels. We applied morphological opening to the cell mask R_{r,v_j} with a disk-shaped structuring element of diameter 5 pixels (~1 µm). This procedure removed thin areas like dendrites but also shrank the soma. Then we applied morphologically dilation with the same structuring element to restore the soma to its original size without restoring the dendrites. The set of on-cell pixels which are not on the soma, S, gives the dendrites. We can now directly calculate the fraction of the cell that is soma as $\frac{\sum_{r_i} I[r_i \in S]}{\sum_{r_i} I\left[R_{r_i,v_j} = 1\right]}$ where $I[\dots]$ is the indicator function.

Spike finding

Identification of action potentials in fluorescence traces is complicated by two factors. The first is temporally uncorrelated photon shot noise; the second is low frequency changes in QuasAr2 baseline caused by photobleaching and blue light crosstalk. Action potentials lie at an intermediate frequency between these two noise sources. To deal with low frequency behavior we employed a specialty percentile filter to approximate the baseline fluorescence around each action potential. The filter identified those points in a sliding window (10 frames, 20 ms long) at the 40th percentile and assigned them baseline status. At points not assigned to the baseline, the local baseline value was inferred via linear interpolation. Signal height was then measured relative to this baseline. We found this method to be more robust than conventional linear filtering in regions of rapid baseline change: near stimulus onset, for example, it creates less "delay" in the baseline estimate while still enabling detection of action potentials.

To handle high frequency noise we set a dynamic threshold. The data were median-filtered (with a window of 400 ms) and the difference between the median and the 16th percentile (i.e. -1σ) was taken as a noise estimate. The threshold for spike detection in the high pass filtered data was set to five times this noise estimate. Our conclusions are robust to changes in this threshold multiplier value. Due to high frequency noise, occasionally the same spike crossed the threshold twice. To avoid double-counting, we set a hard limit on the time between two spikes (no less than 18 ms). We found only a very small number of cases where cells approached this frequency limit.

Once spikes were identified, all further characterization was performed on the original (unfiltered) trace.

Spike parameterization

Spike parameterization is illustrated in Fig. S4 and the approach is justified in Supplemental Discussion. After identifying spikes, we defined windows around each spike on which to perform a functional fit. In the case of an isolated spike, these windows were set to -90 ms and +100 ms from the spike peak. When another spike was within this window, the window was shortened to avoid the neighboring peak. Windows were also truncated to avoid intersection with the stimulus turning on or off.

We fit the pre- and post-peak sections of each action potential separately with a piecewise function with two linear components (termed a "variable hinge"). The function is defined as $f(t) = \begin{cases} y + m_1(t-x) & t \leq x \\ y + m_2(t-x) & t \geq x \end{cases}$. To perform the fit we employed a constrained gradient descent algorithm to minimize least-squares error. Strictly piecewise functions are difficult to optimize, so we approximated $f(t)$ using logistic functions with fast time constants compared to the steepest action potentials. That is, we used $f(t) = y + m_1(t-x)\left(\frac{1}{1+e^{\frac{(t-x)}{\tau}}}\right) + m_2(t-x)\left(\frac{1}{1+e^{\frac{(x-t)}{\tau}}}\right)$, where τ is the timescale of the logistic (set to 2×10^{-6} ms). The error function was a Euclidean norm.

After this initial parameterization, we obtained a model for the baseline fluorescence. We first obtained an approximate estimate of the baseline by removing spikes from the fluorescence trace. Points between the pre- and post-peak time constants of an action potential (that is, near the peak) were removed and replaced with a local linear fit to the five points before and after these boundaries. The remaining baseline dynamics at stimulus on and stimulus off were fit separately with variable hinge models, as above.

In the model of the upstroke, the time coordinate of the meeting point was interpreted as the rise time constant and the y coordinate relative to the local baseline was interpreted as the action potential initiation threshold. In model of the downstroke, the time coordinate of the joint was interpreted as the fall time constant and the y coordinate of the joint relative to the local baseline was interpreted as the after-hyperpolarization. We defined action potential height (in units of $\Delta F/F$) as the distance from the peak of each action potential to the local baseline, divided by the baseline. After-hyperpolarization was similarly defined as the distance from the ΔF coordinate of the hinge point to the local baseline, divided by the baseline.

Statistical methods

In all tests $p < 0.01$ was considered statistically significant. Nonparametric tests were employed to characterize spontaneous firing rates, the distribution of which showed extreme non-normality. Unpaired t-tests were used to compare firing rates under stimulus, where the average number of action potentials produced was much higher than 0 and the statistics were more closely Gaussian. The Holm-Bonferroni method was used to correct for multiple hypothesis testing where appropriate (in particular, choosing between different mechanisms for high-stimulus differences in firing pattern and identifying significant changes in action potential waveform parameters).

A cell was considered to have entered depolarization block at a particular stimulus intensity if it fired its maximum number of action potentials in the previous stimulus epoch, its maximum number of action potentials was higher than three, and in the current stimulus epoch there were fewer action potentials and more than half of those action potentials occurred in the first half of the stimulus epoch. These constraints were constructed to avoid noise from random small differences in spike timing. Cells which never fired more than three action potentials in a single stimulus were considered constitutively inactive and were excluded from further analysis.

To construct a CheRiff level-insensitive measure of activity, we studied the probability of depolarization block at stimulus $n + 1$ conditional on a given number, Y, of action potentials at stimulus n. We call this probability $P(\text{block}_{n+1}|Y_n)$. We started with a dataset consisting of all stimulus epochs from all cells which contained more than three action potentials and which occurred prior to either depolarization block or prior to the last (strongest) stimulus. To avoid sampling errors, we further excluded stimulus epochs which contained the maximum number of action potentials (for that cell) but which were not the first stimulus epoch to do so; these would otherwise create a distortion which would depend on whether the last epoch in which the maximum number of action potentials occurred was the last epoch overall.

To calculate $P(\text{block}_{n+1}|Y_n)$, we employed a generalized linear regression with a binomial distribution and logit linker function, and used cell line (mutant or control), dish recording day (as described in the previous section), the number of action potentials in the current step, and the slope of the F-I curve prior to depolarization block as regression variables. The first two of these variables were treated as categorical. The slope of the F-I curve was included to account for marginal increases in the difference between effective stimulus conductance caused by variations in CheRiff. The given p values come from t-tests on these regression coefficients.

To calculate a CheRiff-independent measure of the maximum firing rate, we took only those cells that entered depolarization block to ensure that the maximum firing rate was reached prior to the strongest optogenetic stimulus. We further excluded cells which fired at their maximum rate for more than one stimulus, again to avoid sampling error. We then fit a linear regression to the maximum firing rates with cell line and dish recording day as categorical (non-interacting) regression variables. The given p values come from t-tests on these regression coefficients.

In our study of differences in action potential waveform, we first averaged together waveform parameters for all action potentials which occurred later than 100 ms after blue light onset within each stimulus epoch (during this initial period the rising baseline caused significant distortion). Our dataset then consisted of waveform parameters from each stimulus epoch that occurred at or before the first maximum in the F/I curve. We employed a linear regression with coefficients for cell line (mutant or control), dish recording day, the number of action potentials in the current step, and the stimulus epoch number (to account for residual distortions caused by blue light cross-talk). The first two variables were treated as categorical. The given p values come from t-tests on these regression coefficients. All statistical analysis was done in MATLAB.

Simulations

We evaluated a Hodgkin-Huxley type model with parameters taken from Powers and co-workers' simulations of human motor neurons (Powers and Heckman, 2015, Powers et al., 2012). (The parameters described in the publications (Powers and Heckman, 2015, Powers et al., 2012) are incorrect and do not give spiking behavior; we instead used the parameters in the associated NEURON simulation files provided in ModelDB). The sodium channel activation parameters were adjusted to reflect the recording temperature in our protocol and the slow inactivation component was dropped for simplicity. K_V-activation parameters in Powers *et al*. were taken from a study (Kuo et al., 2006) in which recordings were performed at the same temperature as in our experiments, and so were not adjusted. Basal K_V7 conductances were doubled from $1\ \mathrm{mS/cm^2}$ to $2\ \mathrm{mS/cm^2}$.

We used the Hodgkin-Huxley equation

$$C_m \frac{dV}{dt} = g_{Na} m^3 h\,(E_{Na} - V) + (g_K n^4 + g_{Kv7} p^4)(E_K - V) + g_m(E_0 - V)$$

Here g_m is a combination of basal leak conductance and CheRiff input conductance. The inactivation particles' time evolution followed the form

$$\frac{dq}{dt} = \frac{q_{inf} - V}{\tau_q}$$

with the parameters

$$\tau_m = \max\left(\frac{1}{0.4\frac{V+33}{1-exp\left(-\frac{(V+33)}{7.2}\right)} - 0.124\frac{V+33}{1-exp\left(\frac{V+33}{7.2}\right)}}, 0.02\right) ms$$

$$m_{inf} = \frac{0.4\frac{V+33}{1-exp\left(-\frac{(V+33)}{7.2}\right)}}{0.4\frac{V+33}{1-exp\left(-\frac{(V+33)}{7.2}\right)} - 0.124\frac{V+33}{1-exp\left(\frac{V+33}{7.2}\right)}}$$

$$\tau_h = \max\left(\frac{1}{0.03\frac{V+48}{1-exp\left(-\frac{(V+48)}{1.5}\right)} - 0.01\frac{V+48}{1-exp\left(\frac{V+48}{1.5}\right)}}, 0.5\right) ms$$

$$h_{inf} = \frac{1}{1+exp\left(\frac{V+53}{4}\right)}$$

$$\tau_n = 1.4 + \frac{11.9 \cdot exp\left(\frac{V+39}{5.5}\right)}{\left(1+exp\left(\frac{V+39}{5.5}\right)\right)^2} ms$$

$$n_{inf} = \frac{1}{1+exp\left(-\frac{(V+25)}{20}\right)}$$

$$\tau_p = 6.7 + \frac{93.3}{exp\left(-\frac{(V+61)}{35}\right) + exp\left(\frac{(V+61)}{25}\right)} ms$$

$$p_{inf} = \frac{1}{1+exp\left(-\frac{(V+61)}{19.5}\right)}$$

where V is in millivolts. The ionic reversal potentials were set to

$$E_{Na} = 50\ mV;\ E_K = -77\ mV; E_0 = E_{ChR} = 0$$

where E_0 is the leak reversal potential and E_{ChR} is the channelrhodopsin (CheRiff) reversal potential. Our model was evaluated in MATLAB using ode15s to handle stiff behavior, with a relative tolerance of 0.003.

Hodgkin-Huxley-type equations model a differential patch of membrane. We sought to account for the effects of variations in cell size and morphology without creating a full compartment or cable model. Since the active channels involved in action potential production are localized, an increase in cell size can produce an increase in total capacitance without a proportional increase in total active channel conductance. We therefore allowed the lumped capacitance C_m to be a tunable parameter and set it to produce maximum firing rates in the range of those seen experimentally (a maximum firing rate before depolarization block of 10-20 action potentials within a 500 ms stimulus); in the simulations shown, it is $20\ \frac{\mu F}{cm^2}$. This represents an effective capacitive load, and is not intended to represent capacitance per geometrical membrane area.

For each set of conductance parameters, we allowed the system to evolve to steady state for 10 seconds prior to delivering stimuli. To identify spikes in the simulation, we looked for peaks 25 mV above the steady-state baseline (obtained via a specialty ordinal filter, as discussed in *Spike finding*). Depolarization block was defined in the same way as in the real data. For step stimulations, the input conductance g_m was turned on with a time constant of 1 ms. When the cell reached steady state (without entering depolarization block) we obtained more precise measurements of firing rate by running the simulation for 2500 ms and then multiplying the number of action potentials found by 1/5 to obtain the expected number of action potentials per 500 ms, as displayed in Fig. 6.

Spike waveforms were parameterized using the same algorithm as was applied to real data. Simulated voltage time traces were down-sampled and their action potentials parameterized using the same models as applied to the real data. We then fit a linear regression on the average waveform parameter from each step with control variables for the channel conductance and the input conductance (Table S3).

Bean, B.P. (2007). The action potential in mammalian central neurons. Nature Reviews Neuroscience *8*, 451-465.

Burnham, K.P. and Anderson, D.R. (2003). Model selection and multimodel inference: a practical information-theoretic approach (: Springer Science & Business Media).

Hyvärinen, A. and Oja, E. (2000). Independent component analysis: algorithms and applications. Neural Networks *13*, 411-430.

Kralj, J.M., Douglass, A.D., Hochbaum, D.R., Maclaurin, D. and Cohen, A.E. (2012). Optical recording of action potentials in mammalian neurons using a microbial rhodopsin. Nat. Meth. *9*, 90-95.

Kuo, J., Lee, R., Zhang, L. and Heckman, C. (2006). Essential role of the persistent sodium current in spike initiation during slowly rising inputs in mouse spinal neurones. J.Physiol.(Lond.) *574*, 819-834.

Mukamel, E.A., Nimmerjahn, A. and Schnitzer, M.J. (2009). Automated analysis of cellular signals from large-scale calcium imaging data. Neuron *63*, 747-760.

Powers, R.K., Elbasiouny, S.M., Rymer, W.Z. and Heckman, C.J. (2012). Contribution of intrinsic properties and synaptic inputs to motoneuron discharge patterns: a simulation study. J.Neurophysiol. *107*, 808-823. Published online Feb. 10.1152/jn.00510.2011 [doi].

Powers, R.K. and Heckman, C.J. (2015). Contribution of intrinsic motoneuron properties to discharge hysteresis and its estimation based on paired motor unit recordings: a simulation study. J.Neurophysiol. *114*, 184-198. Published online Jul. 10.1152/jn.00019.2015 [doi].

Prè, D., Nestor, M.W., Sproul, A.A., Jacob, S., Koppensteiner, P., Chinchalongporn, V., Zimmer, M., Yamamoto, A., Noggle, S.A. and Arancio, O. (2014). A time course analysis of the electrophysiological properties of neurons differentiated from human induced pluripotent stem cells (iPSCs). PloS one *9*, e103418.